

Supporting Information

Amorphous MoO_{3-x} nanosheets prepared by Reduction of crystalline MoO₃ by Mo metal for LSPR and Photothermic Conversion

Cang Guo^{a,#}, Pengfei Yan^{a,#}, Chuanhui Zhu^a, Cong Wei^a, Wei Liu^a, Wenzhuo Wu^a, Xuzhe Wang^a, Lirong Zheng^c, Jiaou Wang^c, Yi Du^d, Jun Chen^e and Qun Xu^{a,b,*}

Materials.

Molybdenum oxide (MoO₃) powder (product number 011837) with the representative lateral size was purchased from Alfa Aesar. Molybdenum (Mo) powder (product number 51014760) was purchased from Sinopharm Chemical Reagent Co., Ltd. (China). Ethanol in analytical grade used in all experiments was purchased from Sinopharm Chemical Reagent Co., Ltd. (China). Deionized water was prepared with double-distilled water. All of the reagents mentioned above were used without further purification.

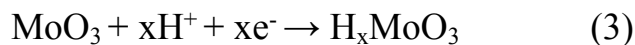
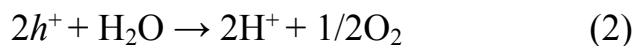
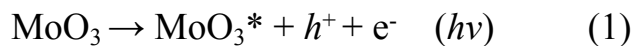
Preparation of pre-irradiation MoO_{3-x} and amorphous MoO_{3-x}.

MoO₃ powder (500 mg) was dispersed in the aqueous solution (100 ml) with ethanol volume fraction of 50% in a 500 ml flask, and the dispersion was ultrasonicated in the bath for 24 h to obtain a homogenous solution

(250 W). Then the solution was centrifuged at 3000 rpm for 45 min to obtain upper supernatant. This light green-blue color supernatant was the prepared ultrasonicated MoO₃. A typical Mo atoms insertion process of amorphous MoO_{3-x} nanosheets sample was as follow, 20 mg Mo metal powder and 80 mg ultrasonicated MoO₃ were mixed with 30 ml deionized water, and transferred into a Teflon-lined stainless steel autoclave (100 ml) and loaded into oven maintaining at 160 °C for 48 h. When the reaction time was up, the autoclave was removed from the oven and cooled to the room temperature naturally. The deep blue mixture solution obtained was irradiated by Xenon lamp at the power of 300 mW cm⁻² for different times (0 h, 1 h, 3 h, 5 h and 7 h), and then all irradiated deep blue solution was centrifuged at 20000 rpm for 15 min to obtained suspensions with different degrees of blue. The corresponding powder (oven; 60 °C) were collected for further characterization. For comparison, the same preparation procedure was conducted, but just no Mo metal powder added into the autoclave.

The hydrogen ions intercalation mechanism.

The intercalation process can be expressed as follows:



Characterization.

The morphologies and microstructures of the prepared samples were analyzed by Tapping-mode AFM (Nanoscope IIIA), Field-emission TEM (JEM-2100) and HRTEM (JEM-2100F). The XRD patterns were examined by Ultima IV instrument. The Raman characterizations were examined by LabRAM HR Evolution with laser wavelength of 532 nm. XPS characterizations were carried out by using ESCLAB 280. UV-vis-NIR spectra were measured by Shimadzu UV-240/PC to evaluate the light adsorption properties. The EPR spectra were collected using a BRUKER EMX plus-9.5/12/P/L electron spin resonance spectrometer at room temperature. X-ray absorption spectroscopy (XAS) and Fourier-transformed extended XAFS (FT-EXAFS) spectra were measured using 1W1B-XAFS experiment station of the Beijing Synchrotron Radiation Facility (BSRF).

Computational details.

The first-principles calculations based on density functional theory were performed by using the CASTEP plane-wave pseudopotential package with Perdew-Burke-Ernzerhof exchange-correlation function. The MoO₃ simulation supercell (Mo₁₆O₄₈) consists of 2*2*1 MoO₃ unit cells of 16 Mo atoms and 48 O atoms. The cutoff energy of the plane-wave basis was 570 eV, for MoO₃ unit cell, 5*2*5 k-points meshes was used for the Brillouin

zone sampling to ensure the accuracy of the calculation results. Moreover, the electron-ion interactions were described by the ultrasoft pseudopotentials (USPPs), and the DFT-D2 method was used for dispersion corrections.

The self-consistent field (SCF) calculation was kept within the energy convergence criterion of 1×10^{-6} eV/atom. In the process of geometric optimization, the total energy converged to 1×10^{-5} eV/atom, and the maximum force converged to 0.03 eV/Å, while the maximum stress converged to 0.05 GPa, and the maximum atom displacement converged to 0.001 Å. All structures including the lattice parameters and the atomic positions were fully optimized by using the BroydenFletcher-Goldfarb-Shanno (BFGS) minimization scheme. The lattice constants of the optimized pristine unit cells of MoO₃ are $a=3.91$ Å, $b=14.2$ Å, $c=3.69$ Å.

Photothermal measurements.

For evaluating the photothermal conversion efficiency of final amorphous MoO_{3-x}, at first the amorphous MoO_{3-x} can be dispersed well in deionized water by ultrasonication to obtain dispersion with different concentrations (0.15 mg ml⁻¹, 0.3 mg ml⁻¹, 0.5 mg ml⁻¹, 0.7 mg ml⁻¹ and 1.0 mg ml⁻¹), and the absorption at 808 nm wavelength of the all dispersion were determined by using UV-visible spectrophotometer (725N). Then 1 ml aqueous dispersion of amorphous MoO_{3-x} (1.0 mg ml⁻¹) were moved into a small

glass bottle with 1.5 ml volume, and irradiated under an 808 nm NIR laser at the power density of 1.06 W cm^{-2} for 720 s. The temperature of the dispersion was real-time measured every 30 s after the start of irradiation via thermocouple temperature probe. After the NIR laser irradiation was shut off, the cooled temperature data was recorded for about 1200 s with the same intervals. In order to investigate the stability of dispersion, six irradiation cycles were conducted under a repeated procedure with laser-on for about 720 s and then laser-off versus time. Deionized water (1 ml) as the control sample and amorphous MoO_{3-x} at other concentrations were measured under the same conditions. Photothermal conversion efficiency (η) of amorphous MoO_{3-x} was calculated according to the Roper's method.

Calculation of the photothermal conversion efficiency.

Following Roper's method and some previous reports, the photothermal conversion efficiency was calculated by Eq (1).

$$\eta = \frac{hA(\Delta T_{max} - \Delta T_{max,H_2O})}{I(1 - 10^{-A\lambda})} \quad (1)$$

Where h is the heat transfer coefficient, A is the surface area of the container, ΔT_{max} and $\Delta T_{max,H_2O}$ are the temperature change of the amorphous MoO_{3-x} dispersion and deionized water at the maximum steady-

state temperature, respectively, I is the 808 nm NIR laser power, and A_λ is the absorbance of the amorphous MoO_{3-x} dispersion at 808 nm wavelength. In this equation, only hA is unknown. So θ is introduced, which is defined as the ratio of ΔT to ΔT_{\max} .

$$\theta = \frac{\Delta T}{\Delta T_{\max}} \quad (2)$$

In addition, the total energy balance of this system as following equation (3).

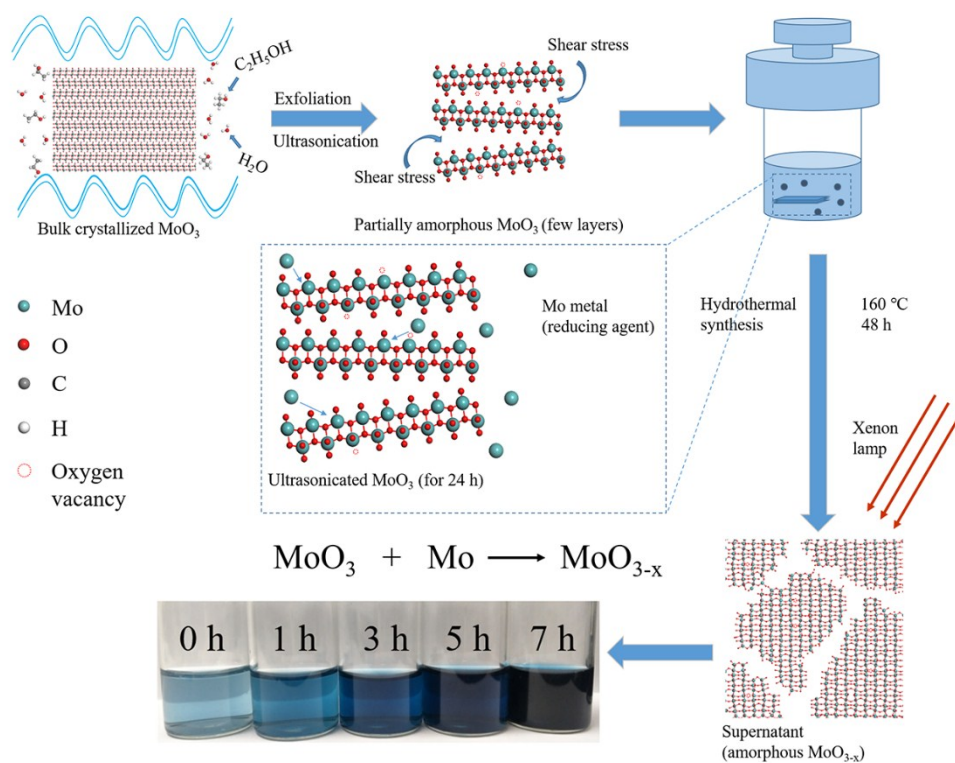
$$\sum_i m_i C_{p,i} \frac{dT}{dt} = Q_A + Q_H - Q_{\text{loss}} \quad (3)$$

Where m and C_p are the mass and heat capacity, respectively. The suffix “i” of m and C_p refers to solvent (water) and dispersed matter (amorphous MoO_{3-x}). T is the solution temperature. Q_A is the photothermal energy absorbed by amorphous MoO_{3-x} per second. Q_H is the heat associated with the light absorbed by water solvent per second. Q_{loss} is the thermal energy lost to the surroundings.

When the laser was shut off, the $Q_A + Q_H = 0$. Substituting equation (2) into equation (3),

$$t = - \frac{\sum_i m_i C_{p,i}}{hA} \ln \theta \quad (4)$$

Where $\frac{\sum_i m_i C_{p,i}}{hA}$ can be calculated by linear relationship of time versus $-\ln \theta$. Mass of amorphous MoO_{3-x} (1×10^{-6} Kg) is far less than that of water solvent (1×10^{-3} Kg), and the specific heat of water is much higher than other materials. Therefore, the m_A and $C_{p,A}$ of amorphous MoO_{3-x} are neglected. $m_{\text{H}_2\text{O}}$ is 1×10^{-3} Kg, $C_{p,\text{H}_2\text{O}}$ is 4.2×10^3 J Kg $^{-1}$ °C $^{-1}$. So hA value can be got in this way, and the photothermal conversion efficiency (η) of amorphous MoO_{3-x} could be calculated.



Scheme S1. Schematic illustration of the fabrication process for the Mo doped amorphous MoO_{3-x} product.

Typically, a simple hydrothermal method designed in this work is schematically illustrated in Scheme S1. First, it is the ultrasonication process. Commercial MoO_3 powder was sonicated in mixed ethanol/ H_2O solvent for 24 h to obtain few-layers MoO_3 , and the shear stress from ultrasonication can help to exfoliate the bulk MoO_3 . For the second step, it is the hydrothermal process. Mo powder was added into dry ultrasonicated supernatant powder in an aqueous solution to reduce MoO_3 into MoO_{3-x} . Simultaneously, amorphous MoO_{3-x} can be obtained with the assistance of high temperature and high pressure. In this process, Mo metal was first

absorbed on the surface of the MoO_3 , and then inserted into the inter-layers, seizing the inherent O atoms of the MoO_3 and resulting in the formation of Mo-Mo metal bonds and the full lattice distortion. When the reaction reached equilibrium and end, the disorder amorphous MoO_{3-x} led by lattice stress and high temperature/pressure was prepared. Finally, it is the irradiation process, under the irradiation of Xenon lamp with a power of 300 mW cm^{-2} , the as-prepared sample solution color changed from original nattier blue to deep blue-black as irradiation time went on. This is the result of hydrogen ions intercalation, and higher free charge carrier concentration prompts the two plasmonic resonance peaks to locate into the visible and near-infrared regions. Hydrogen ions doping leads intrinsic defects and massive electrons into the framework of amorphous MoO_{3-x} , further tailoring the band gaps and oxygen defects.

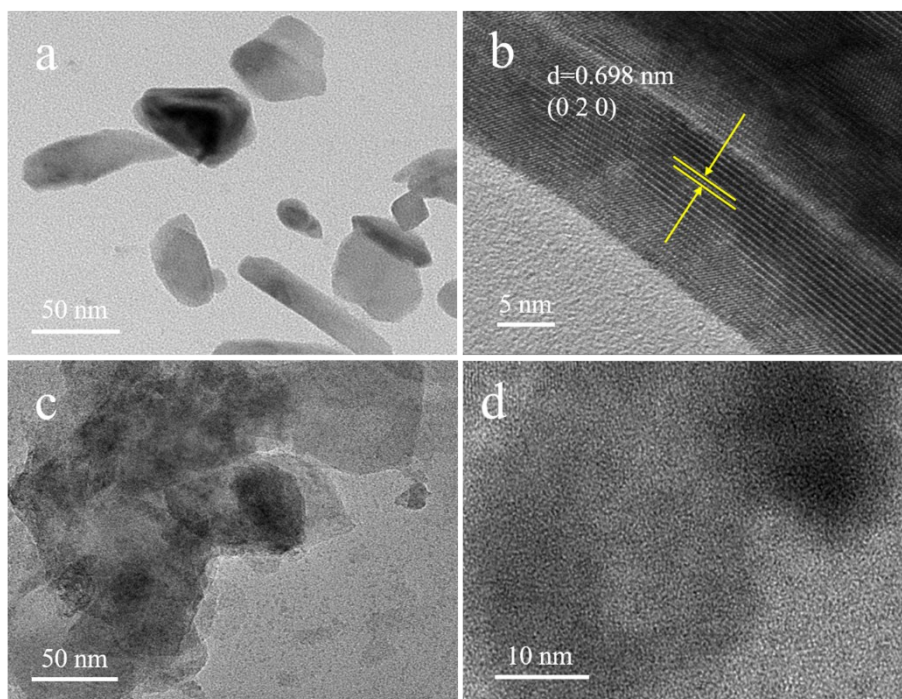
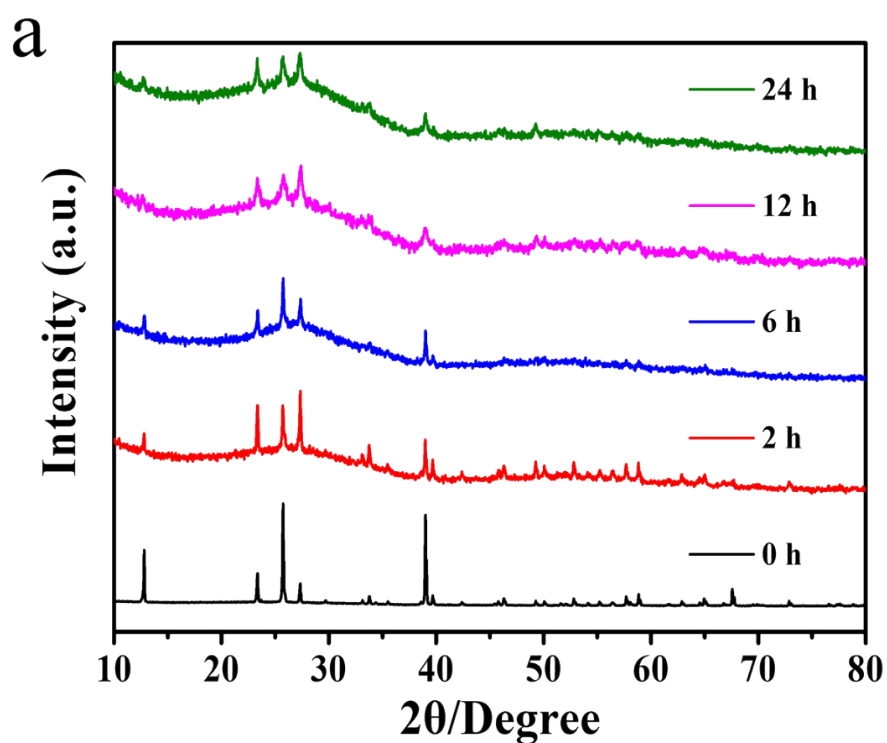


Figure S1. (a, b) TEM images of the ultrasonicated MoO_3 nanosheets. The thickness of one MoO_3 layer is about 0.7 nm in Figure S1b. (c, d) TEM images of the amorphous MoO_{3-x} sample.

The layer spacing of the ultrasonicated sample (Figure S1b) is about 7 Å, indicating the MoO_3 phase as well. The photograph of dry bright-blue powder for amorphous MoO_{3-x} sample is shown in Figure S2c. The size of the nanosheets is around 50 nm wide and 150 nm long (Figure S1c and S1d).



b



c



Figure S2. (a) Wide-angle XRD patterns of the ultrasonicated MoO_3 at different times. (b) Photograph of the ultrasonicated MoO_3 supernatant for 24 h. (c) Bright-blue powder of final amorphous MoO_{3-x} sample.

Commercial α - MoO_3 were ultrasonicated in a mixture of deionized water and ethanol at first. When the ultrasonication time reached 24 h, the

collected supernatant at 3000 rpm exhibited light green-blue color, as shown in Figure S2b. The same XRD peaks for original MoO_3 at other ultrasonication times are shown in Figure S2a. Obviously, the crystallinity of the sample decreases with ultrasonication time extending.

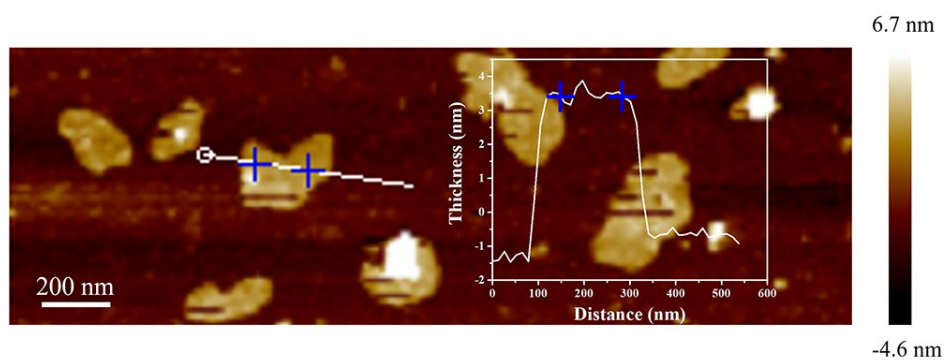


Figure S3. The AFM characterization of amorphous MoO_{3-x} nanosheets.

The atomic force microscopy (AFM) was used for measuring the thickness of amorphous MoO_{3-x} nanosheets, and the thickness is about 4 nm (Figure S3).

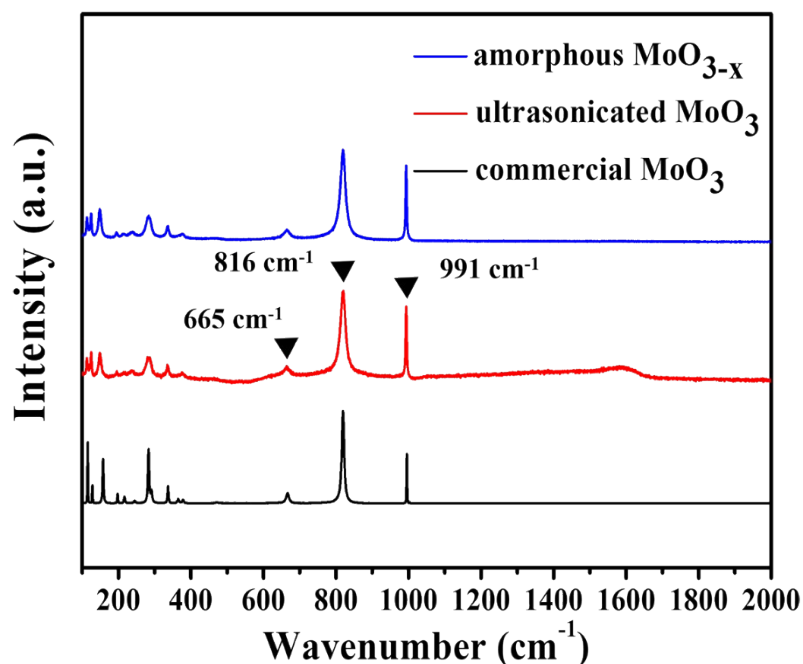


Figure S4. Raman spectra of the amorphous MoO_{3-x}, ultrasonicated MoO₃ and commercial MoO₃.

Raman spectra were carried out to elucidate the composition and structure of the as-prepared MoO_{3-x} sample (Figure S4). As can be seen, several clear peaks located in 665, 816 and 991 cm⁻¹, are all in good agreement with orthorhombic α -MoO₃. The peak located in 665 cm⁻¹ is in good agreement with the bending mode and the stretching mode of the Mo₃-O (the triply coordinated oxygen), which originates from edge-shared oxygen atoms in three adjacent octahedra. While the peak at 816 cm⁻¹ is attributed to the

stretching mode of the Mo₂-O (the bridge oxygen) and the peak at 991 cm⁻¹ is ascribed to the Mo⁶⁺=O (the terminal oxygen) stretching mode.

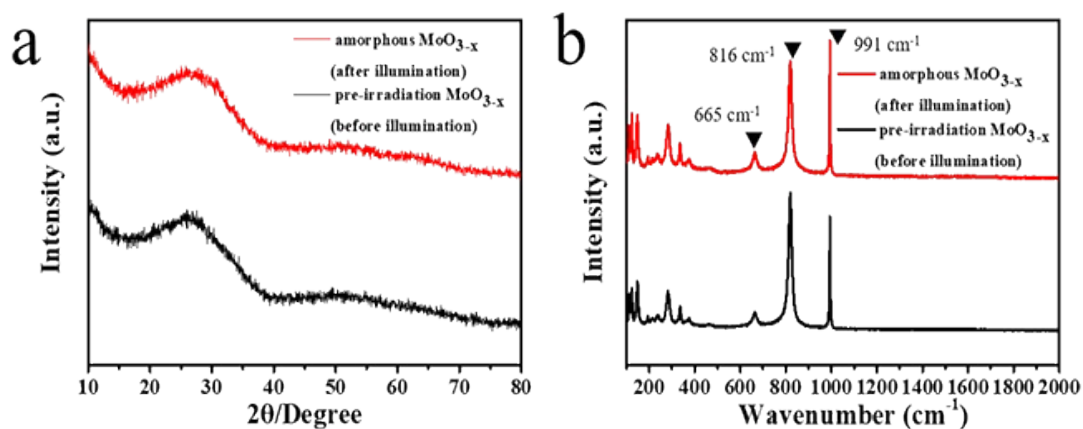


Figure S5. XRD and Raman spectra of pre-irradiation MoO_{3-x} sample.

Compared with XRD and Raman spectra of pre-irradiation MoO_{3-x}, there is no obvious change for the amorphous MoO_{3-x} after illumination (Figure S5).

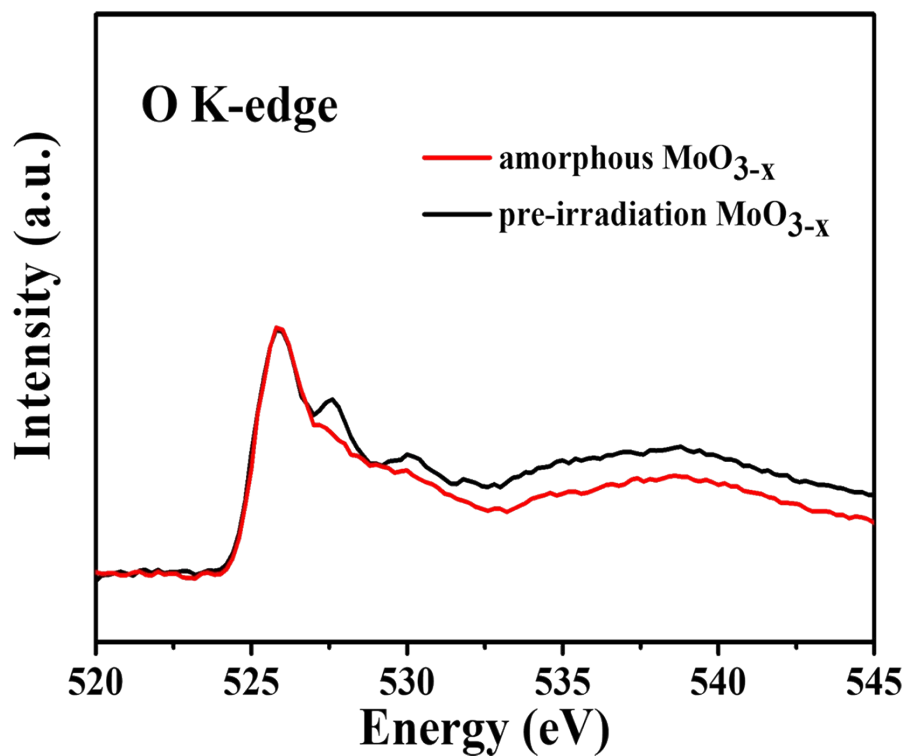


Figure S6. O K-edge XANES spectra for the amorphous MoO_{3-x} sample and the pre-irradiation MoO_{3-x}.

From the O K-edge X-ray absorption near edge structure (XANES) spectra characterization (Figure S6), the decrease of the O K-edge integrated intensity with irradiation by Xenon lamp indicates O content decreases, which is in accordance with the XPS Mo 3d results.

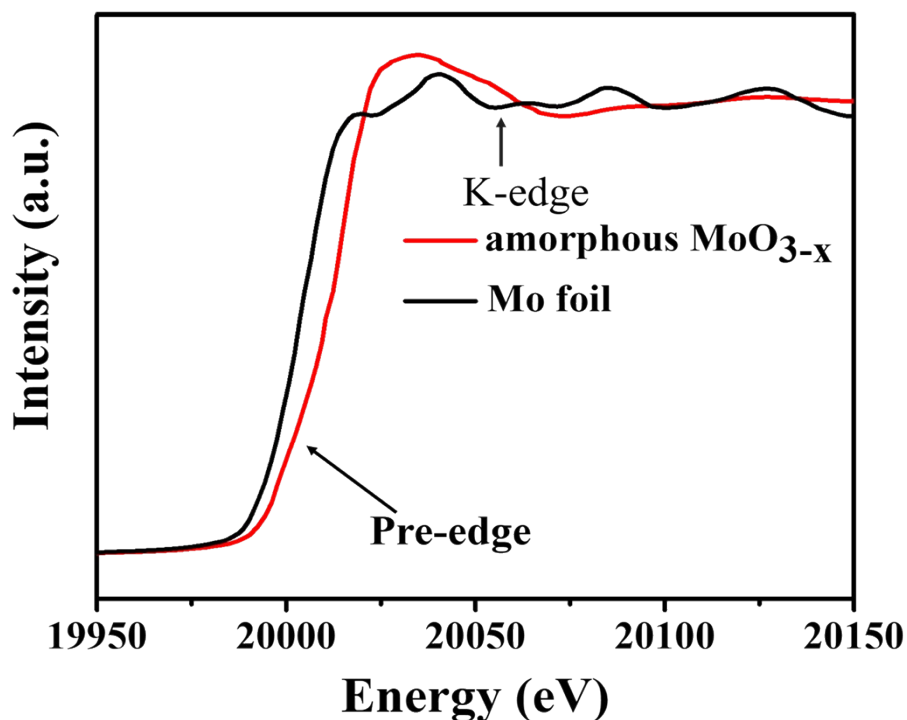


Figure S7. Mo K-edge XANES spectra for the amorphous MoO_{3-x} and the reference material (Mo foil).

The Mo K-edge X-ray absorption near edge structure (XANES) spectra characterization in Figure S7 indicates that the line shapes at the K-edge position could differentiate the assignment of Mo species. As expected, Mo foil as the reference material has lower absorption edge than the amorphous MoO_{3-x}. Furthermore, there is no the pre-edge feature of MoO₃ with Mo⁶⁺ oxidation state in the amorphous MoO_{3-x}. Therefore, the as-prepared amorphous MoO_{3-x} sample is defective and unsaturated, which is

consistent with the EPR results.

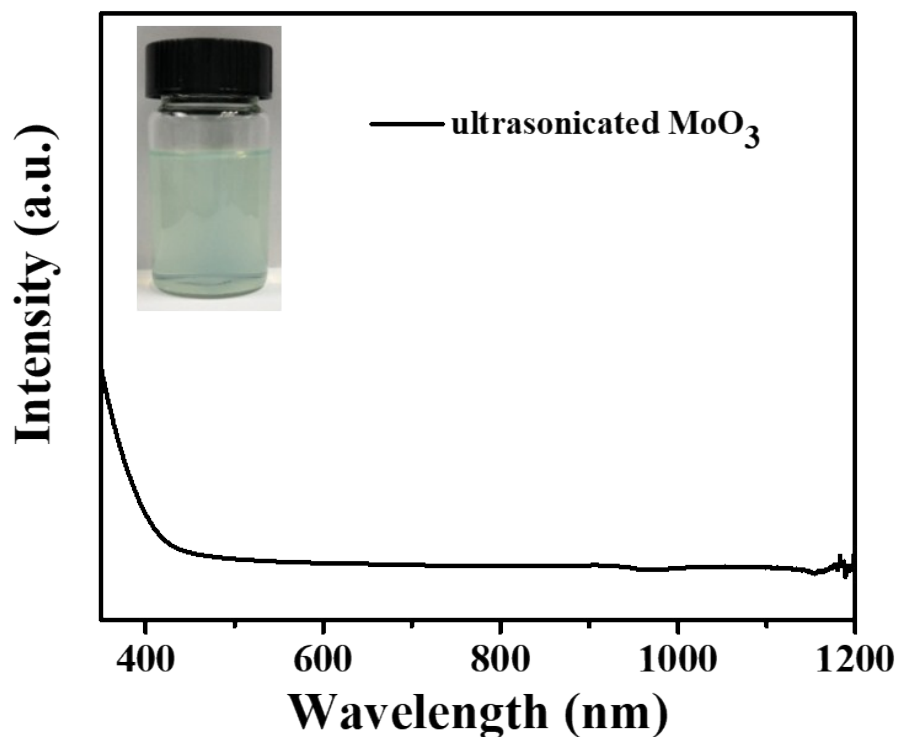


Figure S8. UV/Vis-NIR absorption spectrum of ultrasonicated MoO_3 suspension.

However, for ultrasonicated MoO_3 , there is no peaks of the spectrum in the visible and near-infrared regions (Figure S8), further indicating the successful introduction of defects state in the amorphous MoO_{3-x} . Therefore, this strong near-infrared (NIR) absorption endows the amorphous MoO_{3-x} excellent photothermal performance as a photothermal

agent material driven by 808 nm NIR laser.

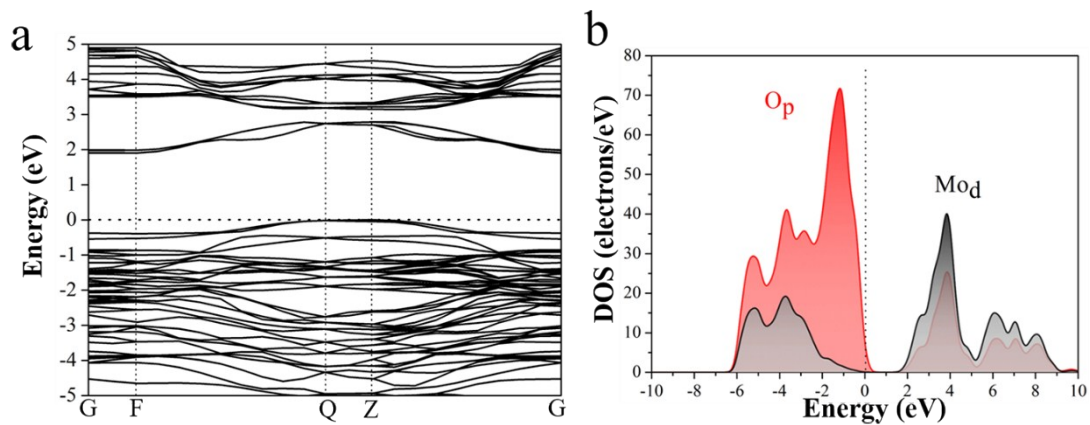


Figure S9. (a) The band structure and (b) density of states of bulk MoO_3 .

In addition, the band gap is 1.9 eV.

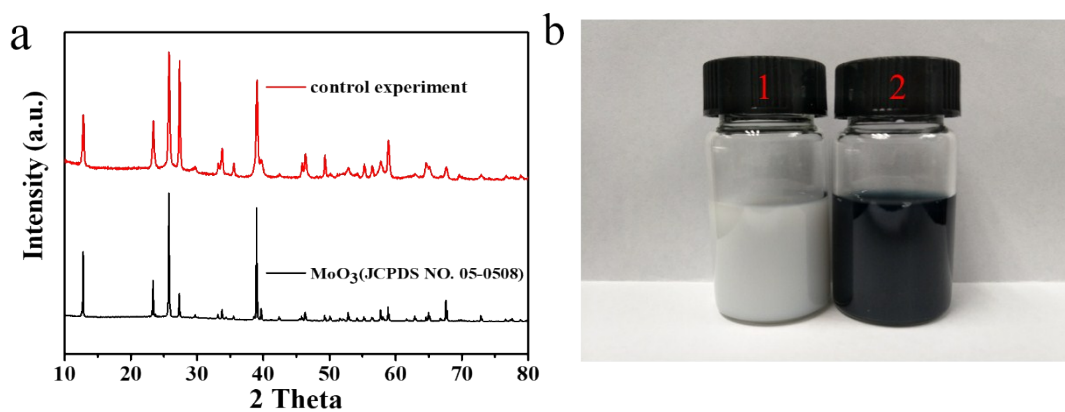


Figure S10. (a) Wide-angle XRD patterns of the recrystallized sample from the control experiment that lacks the reducing agent metal Mo

powder. (b) Photograph of the control experiment sample MoO₃ (number 1) and this work sample MoO_{3-x} (number 2).

To verify the importance of Mo metal powder in this system, the control experiment that only lacks reducing agent Mo powder in the system was carried out. As shown in Figure S10b, the sample solution is ivory-white, which is totally different from the blue-black sample solution. The XRD pattern in Figure S10a indicates that the ivory-white sample is indexed as orthorhombic α -MoO₃ (JCPDS NO. 05-0508), which is the result of the semi-crystallized ultrasonicated MoO₃ recrystallization with the assistance of high temperature and high pressure. In summary, in this designed system, the insertion of Mo atoms is a key factor for the formation of the unique amorphous MoO_{3-x} structure with Mo-Mo bonds.

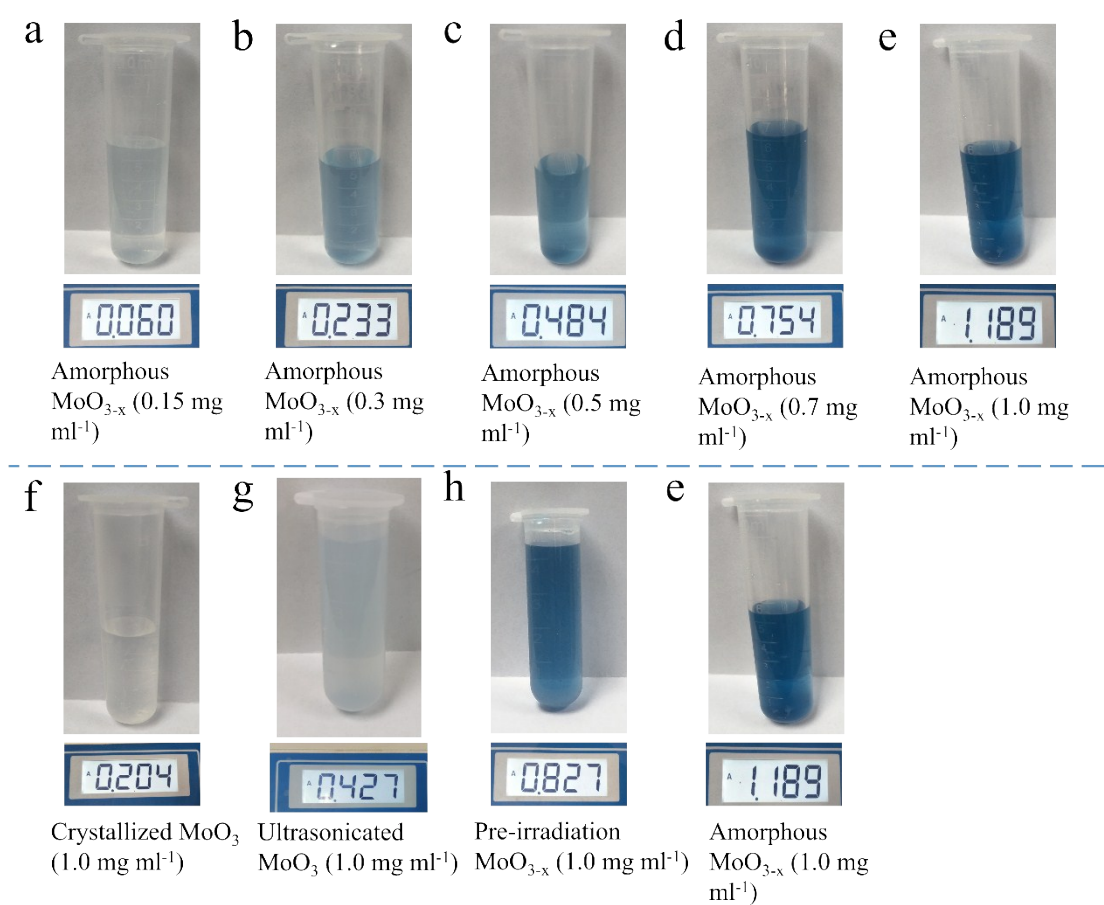


Figure S11. Photographs of various samples solution at different concentrations (a, b, c, d and e) or by different treatments (f, g, h and e), and their corresponding absorbance values at 808 nm wavelength. (measured by single wavelength UV-visible spectrophotometer)

The corresponding absorbance value of various concentration samples solution is shown in Figure S11.

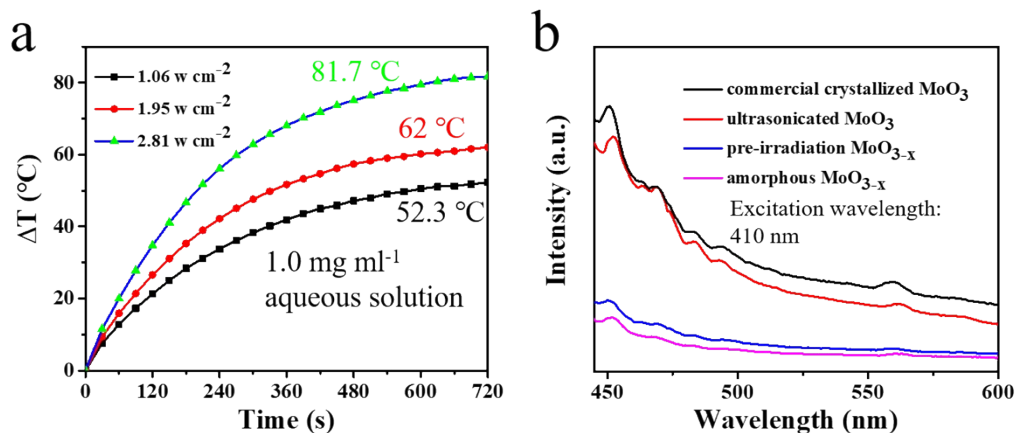


Figure S12. (a) Temperature change of amorphous MoO_{3-x} dispersion at 1.0 mg ml^{-1} concentration with different 808-nm laser powers for 720 s. (b) Fluorescence emission spectra of commercial crystallized MoO_3 , ultrasonicated MoO_3 , pre-irradiation MoO_{3-x} and amorphous MoO_{3-x} .

In addition, as shown in Figure S12a, when the laser power is changed from 1.06 w cm^{-2} to 1.95 and 2.81 w cm^{-2} , the temperature changes are 62 and 81.7°C in 720 s, respectively. Obviously, the higher the laser power, the greater the temperature change.

The photoluminescence (PL) spectra of above samples is shown in Figure S12b, unlike the strong emission of the commercial crystallized MoO_3 and ultrasonicated MoO_3 , the PL emissions of the pre-irradiation MoO_{3-x} and

amorphous MoO_{3-x} are rather weak, which means a fair amount of absorbed photo energy is converted into energy forms other than luminous energy.

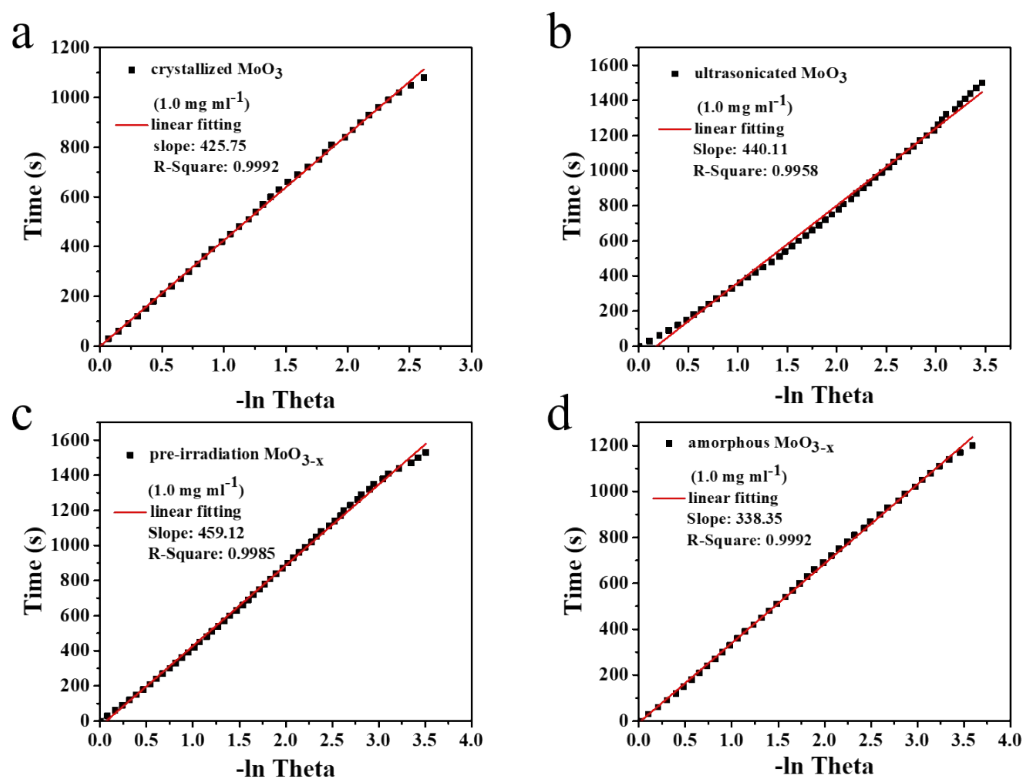


Figure S13. Linear fitting of the cooling time data of the curves of (a) commercial crystallized MoO_3 , (b) ultrasonicated exfoliated MoO_3 , (c) pre-irradiation MoO_{3-x} and (d) amorphous MoO_{3-x} at the same 1.0 mg ml^{-1} concentration vs. the responding negative natural logarithm of the temperature driving force (Θ).

After 720 s of irradiation, the NIR laser was shut off, and the decreased temperature curve was recorded.

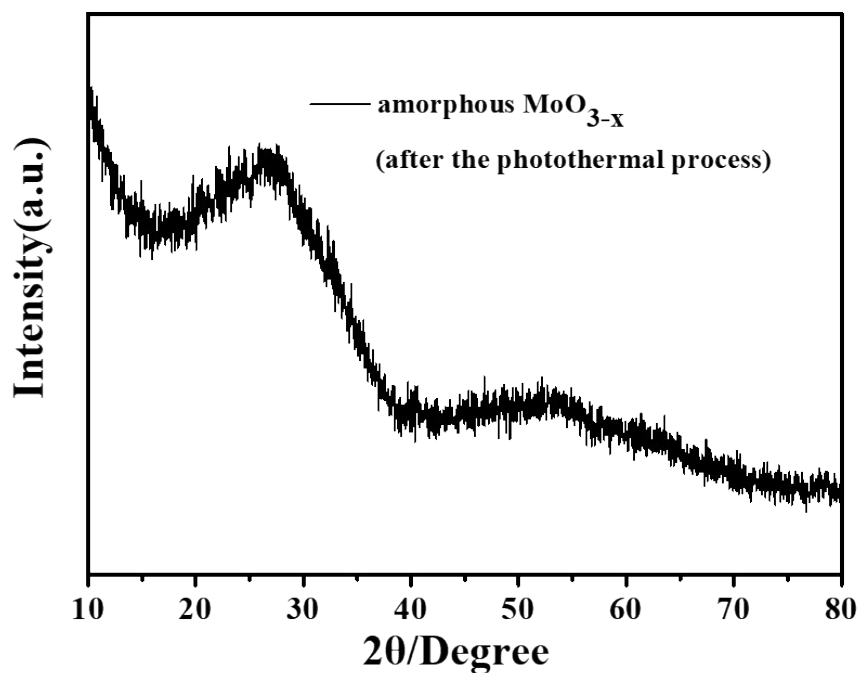


Figure S14. The XRD pattern of the amorphous MoO_{3-x} after the photothermal process.

The stability of amorphous MoO_{3-x} sample is relatively good in the photothermal process. After the photothermal conversion process, the amorphous phase is retained. The corresponding XRD data has been supplied in supporting information.

Table S1. The lattice constants of different configurations.

	Alpha (Å)	Beta (Å)	Gamma (Å)
Model1 (Mo ₁₇ O ₄₈)	7.56	14.29	7.55
Model2 (Mo ₁₇ O ₄₈)	7.73	13.96	7.56
Model3 (Mo ₁₇ O ₄₈)	7.87	13.72	7.49
B-MoO ₃ (Mo ₁₆ O ₄₈)	7.92	13.86	7.40

B-MoO₃ is bulk crystallized MoO₃.

Table S2. The photothermal conversion data of samples solution by different treatments at the same concentration.

sample	ΔT_{\max} (°C)	A_{λ} (808 nm)	h^*A (Time— -ln Theta)	η
Deionized H ₂ O	2.9	0.000	\	\
Commercial MoO ₃	11.9	0.204	0.0099	22.35%
Ultrasonicated MoO ₃	27.8	0.427	0.0095	35.65%
Pre-irradiation MoO _{3-x}	46.8	0.827	0.0091	44.28%

Amorphous MoO _{3-x}	52.3	1.189	0.0124	61.79%
------------------------------	------	-------	--------	--------

Table S3. The photothermal performance of different photothermal agents in recent years.

Photothermal catalyst	PCE	Laser wavelength	references
Au NRs-Cu ₇ S ₄	62%	808 nm	Small, 2018, 14, e1703077.
Dpa-melanin CNSs	40%	808 nm	Adv. Mater., 2013, 25, 1353-1359.
Ultrasmall BPQDs	28.4%	808 nm	Angew. Chem. Int. Ed., 2015, 54, 11526-11530.
Core-shell TiO ₂	55.2%	808 nm	Nanoscale, 2017, 9, 16183-16192.
WO _{2.9}	44.9%	808 nm	Angew. Chem. Int. Ed. 10.1002/anie.201806611.
Ni _x MoO ₃ nanodots	87.4%	808 nm	Chem. Commun., 2019, 55, 9777-9780.
Amorphous MoO _{3-x}	61.8%	808 nm	This work